Organic Process Research & Development

ARTICLE

pubs.acs.org/OPRD

Prediction of Agglomerate Type during Scale-Up of a Batch Crystallization Using Computational Fluid Dynamics Models

Richard F. Falk*

Bend Research, Inc., Bend, Oregon 97701, United States

Ivan Marziano and Terry Kougoulos‡

Pfizer Worldwide Research and Development, Sandwich CT13 9NJ, United Kingdom

Kevin P. Girard

Pfizer Worldwide Research and Development, Groton, Connecticut 06340, United States

ABSTRACT: The impact of hydrodynamics on agglomeration during the crystallization of an active pharmaceutical ingredient (API) was investigated. The type of agglomerate formed was experimentally observed to correlate with agitation level at the laboratory and kilo-lab scales. It was hypothesized that differences in agglomerate type were related to differences in the collision rate of primary crystals, caused by differences in the local degree of agitation (e.g., the local values of fluid turbulence dissipation rate, ε). Spatial distributions of ε were determined from computational fluid dynamics (CFD) models at process scales ranging from laboratory (200 mL) to commercial scale (875 L). Higher values of ε were calculated for conditions shown to result in the formation of rounded, compact agglomerates, while at the lower values of ε, looser agglomerates of flakelike particles were observed. Predictions for pilot-plant- and commercial-scale crystallization operating conditions were made using local ε values as the scaling parameter.

INTRODUCTION

Crystallization is the primary method by which active pharmaceutical ingredients (APIs) are purified and isolated from their reaction mixture in batch processes.[1] Reproducible crystal size and shape during process scale-up are critical from the perspectives of downstream processing, in vivo performance, and regulatory acceptance. During the crystallization process, phenomena such as nucleation, crystal growth, agglomeration, and attrition can change in their relative importance across equipment scales, and thus cause changes in the resulting crystal size distribution and morphology. Generally, agglomeration and attrition have been linked to physicochemical properties of the API and solvent mixture, to the supersaturation during crystallization, and to the hydrodynamics within the reactor.[2] During development and scale-up to commercial manufacturing facilities, the crystallization process is frequently fixed with respect to process type (e.g., cooling vs antisolvent addition) and specific materials (e.g., solvent mixture composition). As a result, any process-related factors that influence agglomeration and attrition may be relatively constant across scales. However, equipment differences and process conditions can have a significant impact on the properties of the isolated solid via differences in fluid dynamics.

The API described in this paper, termed 'compound A', is isolated as agglomerates via a combined evaporative/antisolvent crystallization (solvent removed by distillation and replaced by antisolvent), and the nature of the agglomerates has the potential to impact downstream processing. Initial crystallization process development and optimization work conducted at Pfizer has concluded that compound A crystals can agglomerate into two different morphologies, depending on the crystallizer process conditions. The first type, termed 'loose-flake', is composed of loosely agglomerated flakes with a 2−5 μm primary particle size. The second type, termed 'hard-sphere', has a typically rounded shape, and is harder in nature than "loose-flake" agglomerates, with no distinct primary particle morphology. "Intermediate"-type agglomerates were also observed, although there is no evidence to suggest that a transition from one type of agglomerate to another takes place. The occurrence of each agglomerate type was initially correlated to agitation level at the lab scale. However, subsequent crystallization batches at the larger scale have suggested that an overall measure of agitation such as impeller tip speed is insufficient for the prediction of agglomerate type. Figure 1 show scanning electron micrographs (SEMs) of each type of agglomerate. Figure 1A shows loose-flake agglomerates produced in a pilot-plant-scale reactor and Figure1B shows hard sphere agglomerates produced in a kilo-lab-scale reactor. For this particular compound, loose-flake agglomerates demonstrated improved processability during secondary manufacture and were preferred to hard-sphere particles.

Agglomeration is usually described as a two-step process where particles or crystals collide with a given rate and then

Received: June 6, 2011
Published: October 05, 2011

dx.doi.org/10.1021/op200152u | *Org. Process Res. Dev.* 2011, 15, 1297–1304

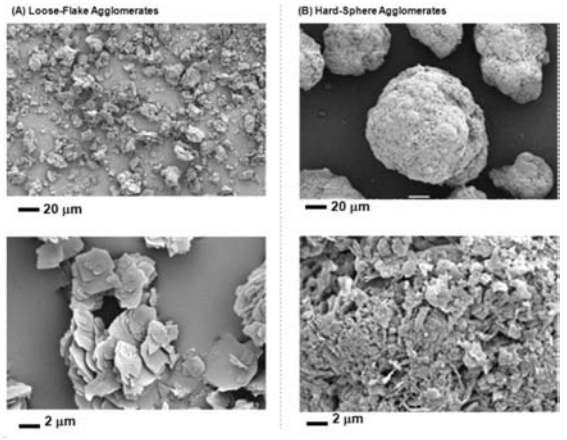

Figure 1. Example SEMs of compound A agglomerate morphology. (A) Flakelike morphology and (B) hard-sphere morphology.

subsequently stick with a given efficiency or probability. This process is described by a second-order rate expression:[1−3]

$$r_{rag} = \beta_{1,2} n_1 n_2 \quad (1)$$

Where n_1 and n_2 represent the number density of crystals of types 1 and 2, respectively. $\beta_{1,2}$ represents an agglomeration rate constant or kernel and can be further decomposed into a crystal−crystal collision rate, N, and agglomeration efficiency, Ψ:[2−4]

$$\beta_{1,2} = \Psi N \quad (2)$$

Many published works have proposed physical mechanisms and quantitative models for both Ψ and N as functions of physicochemical properties of the crystal and solvent,[3,5−10] supersaturation,[3,11] crystal growth rate,[5,7,12] and hydrodynamics of the liquid phase.[3,5,7,13−16] David et al. further subdivided collision and agglomeration rates on the basis of the size of the primary particles into regimes of Brownian, laminar, or turbulence-driven forces.[2] David et al. and Ayazi et al. related collision and attrition mechanisms on the basis of the size of the primary particles compared to the turbulence spectrum;[2,13] that is, different mechanisms were proposed for particle motion in the dissipative vs inertial-convective subranges. Expressions for Ψ and N have been developed that are functions of macroscopic properties of the reactor such as impeller speed or average specific energy dissipation rate.[2,3,13] One potential shortcoming of this approach is that these are quantities that are averaged over the entire volume of the reactor and do not address the inevitable heterogeneities in mixing as the scale of the process increases, as noted by Hounslow and Genck.[3,17] Rielly et al. report Eulerian and Lagrangian simulations of turbulence dissipation rate in a lab-scale, fully baffled stirred tank fitted with a Rushton-style impeller for particle diameters ranging from 20 μm to 2 mm.[18] They show that the Lagrangian probability density functions (pdfs) approach the Eulerian pdfs as the particle diameter decreases. However, the simulations reported in this work suggest that there are differences for particle diameters as small as 5 μm. One potential reason for this apparent discrepancy is that the simulations reported by Rielly and Marquis are for a small-scale, fully baffled tank where the mixing may be more homogeneous compared to the generally unbaffled, larger-scale stirred tanks considered in this work. In addition, the assumption of isotropic turbulence of the k-epsilon models and their variants may be more appropriate for the simulations reported by Rielly and Marquis. Two-equation turbulence models in general, including k-epsilon turbulence models, have been reported to under-predict turbulence quantities for stirred tanks.[19,20] Large eddy simulation (LES) has been reported to be somewhat more accurate for simulating the anisotropic flow in a stirred tank compared to two-equation RANS turbulence models.[20] However, grid size requirements tend to preclude its implementation for routine use at the industrial scale, as recently reported LES simulations of stirred tanks have employed grid sizes of the order of 500,000 to 10 million for reactor volumes ranging from 1 to 20 L.[20−22] A two-equation RANS turbulence model was used in this work in order to provide simulation results within an acceptable simulation time scale. Meroney reports the use of the k-epsilon RANS turbulence model for the successful simulation of an approximately 350-L draft tube reactor and subsequent design of much larger reactors.[23] To address systematic inaccuracy, turbulence quantities are used in conjunction with experiments to determine trends and to rank order reactor conditions. Through computational fluid dynamics reactor models, it is possible to determine not only average, macroscopic mixing performance changes with scale, but also how the spatial distribution of mixing energy (e.g. the local values of turbulence dissipation rate, ε) changes as a function of process conditions and equipment scale.

For the specific case addressed in this work, we have assumed that crystal and solvent properties, and the growth rate are relatively constant across equipment scales, as the crystallization process (e.g., solvent, concentration, mode of supersaturation generation, impurities) remains the same for all batches. Additionally, in situ process monitoring using Mettler Toledo focused beam reflection measurement (FBRM) showed consistency in the onset of crystallization at the scales considered, indicating that supersaturation at that point and in the conditions described here was comparable across scales. The solids content was nominally 4% w/w for all experimental crystallization runs, and simple calculations based on Zwietering's equation[24] show that the particles are suspended and that the agitation rate is greater than 1.3 × N_{JS}, where N_{JS} is the impeller rate required for keeping particles suspended, which is a common criterion for the prediction of homogeneous particle suspension. The implicit assumption is that any change in either Ψ or N is due to differences in reactor hydrodynamics. As a result, we have focused our effort on understanding the difference in hydrodynamics as a function of operating conditions (e.g., impeller speed and fill volume) and equipment scale. The objectives of this study were to (1) quantify differences in hydrodynamics (both macro- and micromixing) between lab-, kilo-lab-, pilot-plant-, and commercial-scale reactors as described in Table 1, (2) correlate those mixing parameters to the type of agglomerate formed, and (3) predict the impact of operating conditions at the commercial scale to control the type of agglomerate obtained.

■ DESCRIPTION OF CRYSTALLIZATION PROCESS AND CFD MODELS

The crystallization of compound A is carried out immediately following the last synthetic step. Formation of hard-sphere agglomerates is observed to occur during a constant volume portion of the crystallization process under conditions of high agitation. As a result, reactors were modeled using a volume and impeller speed corresponding to this period of the crystallization procedure. Since the goal of this work was to characterize and

Table 1. Process settings for CFD simulations

reactor scale	fill volume (L)	impeller speed (rpm)	experimental point	agglomerate type
laboratory	0.2	300	yes	loose flakes
laboratory	0.2	400	yes	loose flakes
laboratory	0.2	600	yes	hard spheres
kilo lab	22	200	yes	hard spheres
pilot plant	170	150	yes	loose flakes
pilot plant	204	150	no	*N/A*
pilot plant	204	125	no	*N/A*
pilot plant	204	100	no	*N/A*
pilot plant	204	75	no	*N/A*
pilot plant	102	150	no	*N/A*
commercial	875	62.5	no	*N/A*
commercial	875	125	no	*N/A*

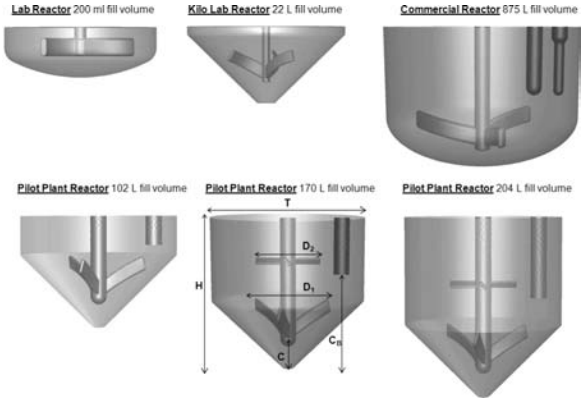

Figure 2. CFD model domains (not to scale).

link crystallization performance to reactor hydrodynamics, simulations where conducted isothermally.

All simulations were developed using single-phase models with a symmetry boundary condition at the liquid surface. The fluid phase density and viscosity were fixed on the basis of the known properties of the solvent used.[25] Model domains were developed and meshed using *Gambit* 2.3.16 commercial CFD meshing software. The model domains consisted of mixed cells of tetrahedral and hexahedral types and ranged in size from approximately 365,000 elements for the lab reactor to approximately 720,000 elements for the commercial reactor. Models were solved using *Fluent* 6.3.26 commercial CFD software using sliding mesh with an unsteady solver. The k-epsilon eddy viscosity turbulence model from Shih et al. (termed the 'realizable k-epsilon turbulence model' within *Fluent*) was used for all simulations.[26] This turbulence model performs similarly to the k-epsilon model of Launder et al. and the RNG k-epsilon model of Yakhot et al., in terms of accuracy, and compares favorably in terms of computational economy.[27−29] It has also been reported to out-perform the standard k-epsilon model for flows with rotation.[30,31] Simulations were conducted on a Linux cluster using between 4 and 8 CPUs, depending on the size of the model.

CFD models were developed for crystallization reactors at lab, kilo-lab, pilot-plant, and commercial scale. Figure 2 depicts the model domains for these different scale reactors. The lab- and kilo-lab-scale reactors were unbaffled, while the pilot-plant- and commercial-scale reactors had either one or two finger-type baffles. The lab-scale reactor had a curved blade turbine impeller, while retreat curve impellers were used in the kilo-lab- and commercial-scale reactors. The lower impeller in the pilot-plant reactor was also a retreat curve impeller, while the upper impeller was a pitched blade turbine (with blades at 45°). Table 1 lists process settings for all of the reactor simulations conducted. In addition, Table 1 also indicates whether each set of conditions corresponds to an experimental crystallization run and which type of agglomerate was observed for those cases. Table 2 lists reactor dimensions.

Table 2. Reactor dimensions

reactor scale	fill volume (L)	T (m)	H (m)	C (m)	C_B (m)	D_1 (m)	D_2 (m)
laboratory	0.2	0.010	0.033	0.015	–	0.073	–
kilo lab	22	0.51	0.25	0.08	–	0.24	–
pilot plant	102	0.68	0.49	0.15	0.36	0.42	–
pilot plant	170	0.68	0.68	0.15	0.36	0.42	0.28
pilot plant	204	0.68	0.78	0.15	0.36	0.42	0.28
commercial	875	1.22	0.86	0.10	0.43	0.92	–

RESULTS AND DISCUSSION

Analysis of the above-listed simulations consisted of both an overall assessment of mixing (e.g., macromixing), and an assessment of differences in local environments (e.g., micromixing) as a function of process conditions and across equipment scales. The overall result of these analyses is the construction of an operating space map that will provide guidance in choosing operating conditions that ensure control over the type of agglomerates formed during subsequent crystallization runs.

Macromixing Performance. Several averaged parameters are typically used to characterize the extent of mixing within a tank and used as scaling parameters. One of these parameters, power/tank fill volume (P/V), is often used as a first-order scaling parameter. For this particular crystallization process, a minimum threshold of P/V is required to suspend the crystals during the growth phase and to disperse thermal gradients from the reactor jacket (although heat transfer was not included in these simulations). For these cases, values of impeller power are obtained directly from the CFD models as the torque required turning the impeller though the fluid using the following:[27]

$$P = 2\pi\omega\tau \tag{3}$$

where

ω = the impeller speed (rps)

τ = the impeller torque obtained from the CFD model ($n-m$)

The power number, N_p, was calculated using:[27]

$$N_P = \frac{P}{\rho_l \omega^3 D_1^5} \tag{4}$$

where

ρ_l = the fluid density (kg/m^3)

D_1 = the diameter of the lower impeller (m)

P/V and N_p obtained from eqs 3 and 4, respectively, are listed in Table 3. The reactor geometry for the pilot-plant reactor at 102 L fill volume (N_p = 0.59) is similar to the reactor studied by Rielly et al., who report a power number from CFD simulations (calculated using impeller torque) of 0.55 vs an experimental

dx.doi.org/10.1021/op200152u |*Org. Process Res. Dev.* 2011, 15, 1297–1304

Table 3. Macromixing performance of reactors

						N_{js} − S = 3 (rpm)		N_{js} − S = 5 (rpm)	
						d_p (μm)		d_p (μm)	
reactor scale	fill volume (L)	impeller speed (rpm)	Re	P/V* (avbW/m^3)	N_p*	5	100	5	100
laboratory	0.2	300	6.0×10^4	258	0.25	96	176	161	292
laboratory	0.2	400	8.1×10^4	660	0.27	96	176	161	292
laboratory	0.2	600	1.2×10^5	2001	0.25	96	176	161	292
kilo lab	22	200	4.7×10^5	530	0.41	34	62	56	103
pilot plant	102	150	9.1×10^5	921	0.59	23	41	38	69
pilot plant	170	150	9.1×10^5	657	0.70	23	41	38	69
pilot plant	204	75	4.5×10^5	76	0.83	23	41	38	69
pilot plant	204	100	6.1×10^5	182	0.78	23	41	38	69
pilot plant	204	125	7.6×10^5	335	0.78	23	41	38	69
pilot plant	204	150	9.1×10^5	654	0.78	23	41	38	69
commercial	875	62.5	2.0×10^6	349	0.52	11	20	19	34
commercial	875	125	4.0×10^6	2896	0.54	11	20	19	34

measurement of 0.41 for a conical bottom reactor with a single beavertail-type baffle and a retreat curve impeller.[30] The difference in H/T and C/T between the reactor in that study ($H/T = 1$, $C/T = 0.16$) versus the one considered in this work ($H/T = 0.72$, $C/T = 0.22$) may account for the difference between calculated values of the power number. Thus, CFD calculations of overall power draw are generally consistent with that data, albeit over-predictive in both studies.

P/V obtained from eq 3 was compared to P/V obtained from volume averaged turbulence dissipation rate multiplied by fluid density. In all cases, P/V from turbulence dissipation rate was approximately 4 times lower than P/V obtained from impeller torque. Figure 3 shows a parity plot of P/V obtained from the two different methods. Figure 3 shows that while the turbulence dissipation rate may be substantially under-predicted with Shih's k-epsilon model, the averaged values are linearly correlated to P/V from impeller torque, and useful for rank-ordering reactor conditions.

In addition to P/V, the 'just-suspended impeller speed', N_{js}, was estimated using eq 5:[24]

$$N_{js} = S\upsilon^{0.1}\left(\frac{g(\rho_s - \rho_l}{\rho_l}\right)^{0.45} X^{0.13} d_p^{0.2} D^{-0.85} \quad (5)$$

where

ν = fluid kinematic viscosity at 80 °C (2.8×10^{-7} m^2/s)[22]
g = gravitational constant (9.81 m/s^2)
ρ_s = density of solid (1400 kg/m^3)
ρ_l = density of liquid (783 kg/m^3)
X = mass loading of solids (4 kg/100 kg)
d_p = particle diameter (5×10^{-6}, 1×10^{-4} m)
D = impeller diameter (0.073 m for lab, 0.24 m for kilo lab, 0.42 m for pilot plant, 0.92 m for commercial)
S = a constant determined by the impeller type and tank configuration.

Values of the eq 5 quantities used to calculate N_{js} as reported in Table 3 are listed in parentheses above. A range of S values (3−5) was used to estimate N_{js} for the conditions modeled for each of the different reactor scales as determined by Rielly et al. for crystallizers with retreat curve impellers and a single beavertail baffle.[32] Particle diameters of 5 and 100 μm were used for the calculations to represent the approximate size of the primary particle and a worst-case scenario during crystal growth and subsequent formation of agglomerates, respectively. Values of N_{js} should be considered estimates only due to the assumed values for particle diameter and the values of S. Table 3 summarizes estimates of N_{js} from eq 5 for all simulations. The N_{js} calculations suggest that all of the conditions in Table 3 should provide sufficient agitation to suspend both primary crystals and the agglomerates.

Micromixing Performance. Micromixing analysis can be used to characterize interactions at the smallest length scale within a tank (e.g., the length scale at which particle collisions may occur). It can also be used to quantify the distribution of these mixing parameters within a tank (e.g., mixing heterogeneities). One important quantity used to characterize micromixing is the fluid turbulence dissipation rate (ε). ε provides an estimate of the smallest eddy size that exists within a turbulent flow via the Kolmogorov length scale.[33,34]

$$\lambda_k \approx \left(\frac{\nu^3}{\varepsilon}\right)^{1/4} \quad (6)$$

where

ν = kinematic fluid viscosity (m^2/s)
ε = turbulent dissipation rate (m^2/s^3)

As λ_k decreases due to more vigorous mixing, crystals that are circulating within these eddies can become spatially closer to each other and may possess a higher relative velocity to each other which may, in turn, increase the crystal−crystal collision rate. The local value of ε encountered by crystals as they circulate throughout a fluid has been linked to the crystal−crystal collision rate. For the case where the crystal diameter is small compared to λ_k, Saffman et al. derived the following equation to describe the crystal−crystal collision rate, N.[35]

$$N = 1.3 d_{12}^3 n_1 n_2 \left(\frac{\varepsilon}{\nu}\right)^{1/2} \quad (7)$$

where

d_{12} = the sum of diameters of particles 1 and 2 (assumed 5 μL)
n_i = the number density of particle 1 or 2 (no./m^3)

dx.doi.org/10.1021/op200152u |Org. Process Res. Dev. 2011, 15, 1297–1304

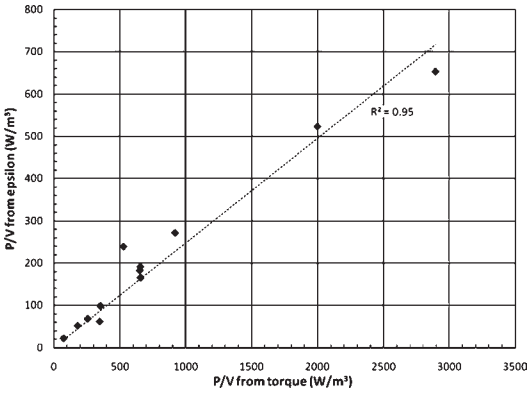

Figure 3. Parity plot of P/V obtained from impeller torque vs turbulence dissipation rate.

ε = turbulence dissipation rate (m^2/s^3)
ν = kinematic fluid viscosity (m^2/s)

Simulation results indicate that λ_k is on the order of 20−30 μm, suggesting that eq 7 is a better approximation for the collision rate of primary crystals (typical size <5 μm) than the treatment proposed by Abrahamson where the collision rate is determined from the crystal−fluid slip velocity.[36] If it is assumed that crystal size, number density, and fluid viscosity do not change significantly across scales, then the crystal−crystal collision rate increases as the crystals experience a higher degree of fluid turbulence. The small fraction of crystals experiencing these high levels of fluid turbulence will have a higher probability of colliding and forming hard-sphere agglomerates compared to crystals in reactor regions and conditions of lower fluid turbulence. For the purpose of this work, the impact of changes in fluid turbulence on collision efficiency is neglected. Although work by Liew et al. indicates that for low efficiencies ψ is proportional to ε^{-1},[37] and therefore differences in collision efficiencies across scales/conditions can be expected, the results presented here show that a framework for the prediction of agglomerate type as a function of hydrodynamics can be based on dependence from collision rates alone.

CFD simulations were conducted using the discrete phase model within *Fluent* 6.3.26 (termed 'DPM") for all the conditions from Table 1 wherein a discrete solid phase of a prescribed diameter and density (e.g., 'crystals') were spatially tracked within a reactor.[38] Fluent's DPM is a dilute Lagrangian−Eulerian tracking scheme with one-way momentum coupling using a discrete random walk to account for fluid velocity fluctuations. As a one-way coupled simulation, fluid turbulence augmentation from the discrete phase was not included. The volume fraction of the discrete phase (e.g., the crystal phase) in the process being simulated is approximately 0.05−0.07, suggesting that one-way coupling may be sufficient. Clearly, two-way momentum coupling as well as particle−particle collisions will provide a higher level of resolution in terms of agglomerate size and growth rates as illustrated by Gimbun et al.[39] A primary goal of the CFD simulations for this study was to help identify the hydrodynamic conditions which would promote one type of agglomerate over another type, and not necessarily to simulate the agglomerate growth process. The crystals were modeled using a diameter of 5 μm and a density of 1.4 g/cm^3. As the crystals are tracked, their history of exposure to the fluid's turbulence dissipation rate is recorded and converted into a histogram of the fraction of time

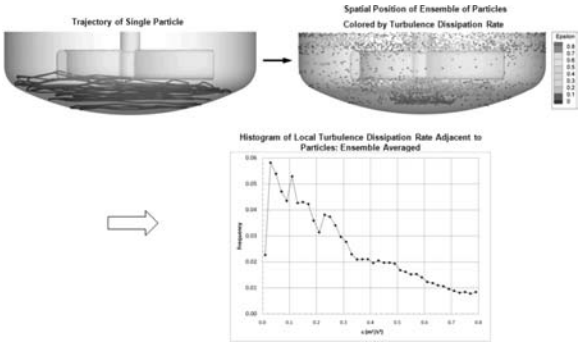

Figure 4. CFD modeling procedure to obtain particle turbulent dissipation rate history.

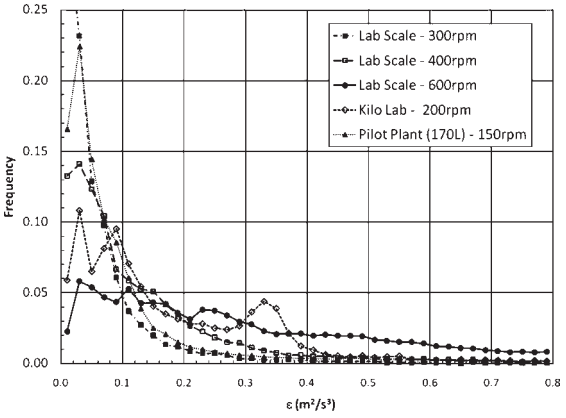

Figure 5. Turbulence dissipation rate histograms for lab-, kilo-, and pilot-plant-scale CFD simulations corresponding to experimental crystallization runs.

spent at each level of turbulence dissipation rate using a user-defined function within *Fluent*. Figure 4 schematically depicts this process. For example, from the histogram in Figure 4, the suspended crystals spend approximately 3% of their time exposed to fluid with a turbulence dissipation rate of 0.3 m^2/s^3. The local turbulence values (e.g., the history of turbulence dissipation rate experienced by the crystals) are important for estimating particle−particle collision rates in that those values provide a description of how individual crystals are moving relative to each other. This relative motion of crystals as described by ε in eq 7 contributes to crystal−crystal collisions, and subsequent agglomeration. Figure 5 overlays histograms of turbulence dissipation rate exposure for simulations corresponding to the five experimental conditions listed in Figure1. Significant differences are evident in the upper tail of the distributions for the two cases for which hard-sphere agglomerates were observed, suggesting differences in the exposure history of crystals to fluid turbulence.

The collision rate in eq 7 was calculated for the simulations corresponding to experimental crystallization runs using mean values of $\varepsilon^{1/2}$ obtained from particle tracking simulations described above using the following:

$$\langle \varepsilon^{1/2} \rangle = \sum_{i=1}^{k} f_i \varepsilon^{1/2} \tag{8}$$

where f_i is the frequency of ε in the ith bin of the histogram of ε containing k bins. These rates were also normalized to the

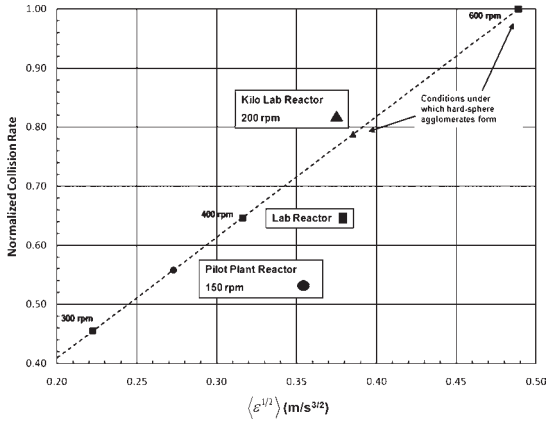

Figure 6. Normalized crystal−crystal collision rate vs $\langle \varepsilon^{1/2} \rangle$.

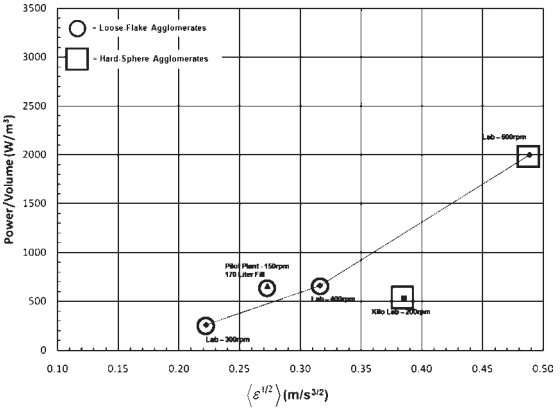

Figure 7. P/V vs $\langle \varepsilon^{1/2} \rangle$. Points in Figure 7 are for simulations for which experimental observations of agglomerate morphology exist.

collision rate for the 600 rpm lab reactor case. These results are plotted in Figure 6 along with eq 7, also normalized to the collision rate for the 600 rpm lab reactor case since the remaining terms in eq 7 are assumed constant across all conditions. Simulations of the lab reactor at 600 rpm and the kilo-lab reactor at 200 rpm resulted in the highest values of crystal−crystal collision rates and would appear to be most prone to agglomeration from collisions. These calculations are consistent with experimental results (as noted within Figure 6).

From this analysis, an intermediate conclusion is that the energy imparted to the fluid must be relatively evenly distributed. That is, there should be minimal "hot spots" of locally high turbulence levels that the suspended crystals encounter. From conventional mixing analysis, however, it is known that there is a minimum amount of overall mixing energy required to adequately mix the liquid and to suspend the growing crystals. To help quantify the balance between sufficient macromixing and uniform micromixing, Figure 7 plots the calculated values of P/V vs $\langle \varepsilon^{1/2} \rangle$ for the five simulations for which experimental crystallizations runs have been conducted. The type of observed agglomerates is called out in the figure. For the five conditions and reactors modeled in Figure 7, there was no experimental indication of insufficient macromixing (e.g., there was no observation of the tendency for settling of crystals). Therefore, on the basis of experimental results and CFD simulations, the

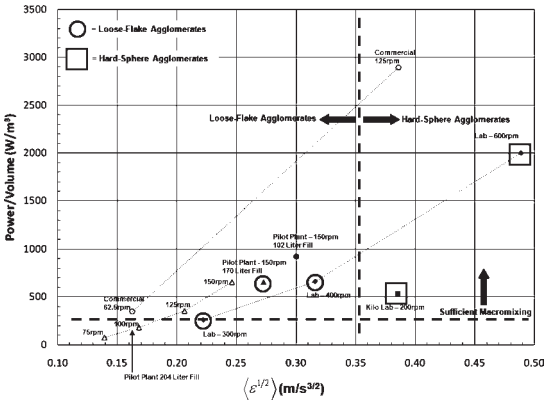

Figure 8. P/V vs $\langle \varepsilon^{1/2} \rangle$. Points in the plot are for all simulations conducted; those corresponding to actual experimental points are highlighted by a square or circle, depending on the type of agglomerate observed.

minimal P/V for adequate macromixing is estimated to be no higher than approximately 260 W/m^3 for 5 μm particles (the lowest P/V values for which experimental data exist—the lab-scale vessel at 300 rpm). In addition, values of $\langle \varepsilon^{1/2} \rangle$ greater than approximately 0.35 m/s$^{3/2}$ resulted in hard-sphere agglomerates. These simulations and experiments indicate that scaling up the crystallization process solely by a macromixing parameter such as P/V is insufficient for choosing conditions that result in the loose-flake agglomerate. From Figure 7, the value of P/V for the kilo-lab run (where hard, spherical agglomerates were observed) is lower than P/V values for either the pilot-plant reactor at 150 rpm or the lab reactor at 400 rpm—conditions for which loose-flake agglomerates were observed. Thus, it is not only the mean level of agitation that is important but also the spatial distribution of mixing energy throughout the reactor that are encountered by growing crystals.

The increase in collision rate with increasing agitation must also change the relative importance of nucleation, crystal growth, and agglomeration processes in determining crystal size, shape, and hardness of the agglomerates formed during the process. In particular, we hypothesize that, at the higher level of agitation, both nucleation and agglomeration are faster than crystal growth, resulting in the loss of the characteristic flake particle shape observed at the lower agitation rates, and the residual supersaturation is consumed for the formation of solid bridges that hold the spherical agglomerates together, thus explaining the harder nature of these compared to that of the "flakelike" agglomerates. In addition, while only two types of agglomerates are described here for simplicity, in reality there is a continuum of particle types that encompasses the two morphologies described here.

Additional simulations were conducted for the pilot-plant- and commercial-scale reactors in order to provide recommendations for operating conditions for future crystallization runs. Pilot-plant simulations were conducted with varying fill volumes and varying impeller speeds. Commercial simulations were conducted with a single fill volume of 875 L with impeller speeds of either 62.5 or 125 rpm (the two possible impeller speeds available for the commercial-scale reactor). Tables 1 and 2 list the specific conditions for both the pilot-plant and commercial simulations. Macromixing and micromixing analyses similar to those reported in Figure 7 were conducted on these simulations. These additional simulation results are shown in Figure 8. Figure 8

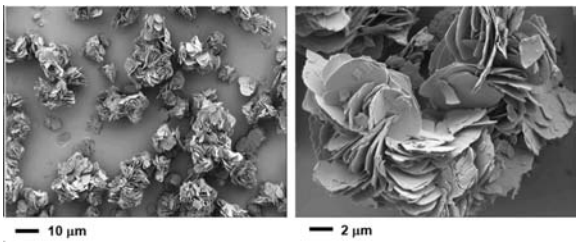

Figure 9. SEMs of agglomerates from pilot-plant scale at 204-L fill volume and 125 rpm impeller speed.

also begins to delineate the plot into an operating space map. Figure 8 shows that impeller speeds below 125 rpm for the pilot-plant reactor may begin to show insufficient macromixing. For the commercial reactor, an impeller speed of 62.5 rpm will likely produce flakelike agglomerates, while 125 rpm will likely produce the hard-sphere type. Using 62.5 rpm as the target conditions for the final commercial process, it was recommended that any subsequent pilot-plant runs be conducted at 125 rpm with a fill volume of 204 L to most closely match both macro- and micromixing environments at the commercial scale. Figure 9 below shows SEM photomicrographs for a subsequent crystallization run at the pilot-plant scale using the operating conditions as recommended above (204-L batch size, 125 rpm impeller speed). Figure 9 indicates that the desired, flakelike agglomerates were produced under these operating conditions, consistent with the predicted operating space shown in Figure 8.

CONCLUSIONS

From this work, a correlation has been developed between the turbulence dissipation rate experienced by growing crystals of compound A and their tendency to agglomerate into a spherical morphology. A physical explanation for this correlation is hypothesized to be an increase in crystal−crystal collisions in regions of the reactor of higher fluid turbulence, promoting the formation of the spherical agglomerates. From this analysis and from conventional macromixing analysis, a preliminary operating space map was constructed for reactors ranging from lab scale to commercial scale. A crystallization run conducted at the pilot-plant scale was used to help validate this operating space map. In addition, on the basis of these models, conditions were identified for commercial-scale production that should ensure consistency in the type of crystal agglomerate formed for each batch.

As indicated in the main body of the article, the prediction of agglomeration type was essentially related to the particle−particle collision rate, while the impact of hydrodynamics on collision efficiency was neglected. Although the results demonstrate that the framework adopted produces a fit-for-purpose predictive model, an extension of this work could entail the inclusion of the impact of hydrodynamics on collision efficiency, specifically through relating the type of agglomerate observed to the overall agglomeration rate—that is, including the effects of both collision rate and collision efficiency.

AUTHOR INFORMATION

Corresponding Author
falk@bendres.com

Present Addresses
[‡]Novan Inc., Durham, NC 27703

ACKNOWLEDGMENT

We gratefully acknowledge Fluent Inc. for providing the User-Defined Function used to track turbulence history of the discrete phase model and Prof. Michael Hounslow for feedback on the manuscript. In addition, Keith Horspool, Ruth Hardy, Deirdre O'Brien, and Radoslav Penchev of Pfizer Worldwide Research and Development, and Elizabeth Ortiz of Pfizer Global Supply are thanked for support and technical discussions.

REFERENCES

(1) Tung, H.-H.; Paul, E. L.; Midler, M.; McCauley, J. A. *Introduction to Crystallization Issues*; John Wiley & Sons, Inc.: New York, 2008; pp 1−11.

(2) David, R.; Espitalier, F.; Cameriao, A. Developments in the Understanding and Modeling of the Agglomeration of Suspended Crystals in Crystallization Solutions. *KONA* **2003**, *21*, 40–53.

(3) Hounslow, M. J.; Mumtaz, H. S.; Collier, A. P.; Barrick, J. P.; Bramley, A. S. A Micro-Mechanical Model for the Rate of Aggregation during Precipitation from Solution. *Chem. Eng. Sci.* **2001**, *56* (7), 2543–2552.

(4) Mersmann, A. *Crystallization Technology Handbook*, 2nd ed.; Marcel Dekker: New York, 2001.

(5) Ålander, E. M.; Rasmuson, Å. C. Mechanisms of Crystal Agglomeration of Paracetamol in Acetone−Water Mixtures. *Ind. Eng. Chem. Res.* **2005**, *44* (15), 5788–5794.

(6) Ålander, E. M.; Rasmuson, Å. C. Agglomeration and Adhesion Free Energy of Paracetamol Crystals in Organic Solvents. *AIChE J.* **2007**, *53* (10), 2590–2605.

(7) Ilievski, D.; Livk, I. An Agglomeration Efficiency Model for Gibbsite Precipitation in a Turbulently Stirred Vessel. *Chem. Eng. Sci.* **2006**, *61* (6), 2010–2022.

(8) Kuboi, R.; Nienow, A. W.; Conti, R. Mechanical Attrition of Crystals in Stirred Vessels. *Ind. Cryst.* **1984**, *2*, 211–216.

(9) Nyvlt, J. S.; Sohnel, O.; Matuchova, M.; Broul, M. *The Kinetics of Industrial Crystallization*; Elsevier: New York, 1985.

(10) Synowiec, P.; Jones, A. G.; Ayazi Shamlou, P. Crystal Break Up in Dilute Turbulently Agitated Suspensions. *Chem. Eng. Sci.* **1993**, *48* (20), 3485–3495.

(11) David, R.; Marchal, P.; Marcant, B. Modelling of Agglomeration in Industrial Crystallization from Solution. *Chem. Eng. Technol.* **1995**, *18* (5), 302–309.

(12) Madras, G.; McCoy, B. J. A Fragmentation Model for Crystal Attrition. *J. Cryst. Growth* **2007**, *305* (1), 211–217.

(13) Ayazi Shamlou, P.; Jones, A. G.; Djamarani, K. M. Attrition of Potassium Solphate Crystals in Stirred Vessels. *IChemE Symp.* **1990**, *121*, 309–323.

(14) Evans, T. W.; Sarofim, A. F.; Margolis, G. Models of Secondary Nucleation Attributable to Crystal-Crystallizer and Crystal-Crystal Collisions. *AIChE J.* **1974**, *20* (5), 959–966.

(15) Ramshaw, C. Secondary Nucleation in Mechanically Agitated Crystallizers: Crystal Motion in the Impeller Region. *Chem. Eng.* **1974**, No. July-August, 446–449.

(16) Yu, Z. Q.; Tan, R. B. H.; Chow, P. S. Effects of Operating Conditions on Agglomeration and Habit of Paracetamol Crystals in Anti-solvent Crystallization. *J. Cryst. Growth* **2005**, *279* (3−4), 477–488.

(17) Genck, W. Understanding Crystallization. *Chem. Eng. Prog.* **2008**, No. February, 22–24.

(18) Rielly, C. D.; Marquis, A. J. A Particle'S Eye View of Crystallizer Fluid Mechanics. *Chem. Eng. Sci.* **2001**, *56* (7), 2475–2493.

(19) Li, M.; White, G.; Wilkinson, D.; Roberts, K. J. LDA Measurements and CFD Modeling of a Stirred Vessel with a Retreat Curve Impeller. *Ind. Eng. Chem. Res.* **2004**, *43* (20), 6534–6547.

(20) Yeoh, S. L.; Papadakis, G.; Yianneskis, M. Numerical Simulation of Turbulent Flow Characteristics in a Stirred Vessel Using the LES and RANS Approaches with the Sliding/Deforming Mesh Methodology. *Chem. Eng. Res. Des.* **2004**, *82* (7), 834–848.

(21) Bakker, A.; Oshinowo, L. M. Modelling of Turbulence in Stirred Vessels Using Large Eddy Simulation. *Chem. Eng. Res. Des.* **2004**, *82* (9), 1169–1178.
(22) Hartmann, H.; Derksen, J. J.; Montavon, C.; Pearson, J.; Hamill, I. S.; van den Akker, H. E. A. Assessment of Large Eddy and RANS Stirred Tank Simulations by Means of LDA. *Chem. Eng. Sci.* **2004**, *59* (12), 2419–2432.
(23) Meroney, R. N.; Colorado, P. E. CFD Simulation of Mechanical Draft Tube Mixing in Anaerobic Digester Tanks. *Water Res.* **2009**, *43* (4), 1040–1050.
(24) Zwietering, T. N. Suspending of Solid Particles in Liquid by Agitators. *Chem. Eng. Sci.* **1958**, *8* (3−4), 244–253.
(25) Perry, R. H.; Green, D. W. *Perry's Chemical Engineers' Handbook*, 6th ed.; McGraw-Hill: New York, 2008.
(26) Shih, T.-H.; Liou, W. W.; Shabbir, A.; Yang, Z.; Zhu, J. A New k-[epsilon] Eddy Viscosity Model for High Reynolds Number Turbulent Flows. *Comput. Fluids* **1995**, *24* (3), 227–238.
(27) Aroussi, A.; Kucukgokoglan, S.; Pickering, S. J.; Menacer, M. In *Evaluation of Four Turbulence Models in the Interaction of Multi Burners Swirling Flows*; 4th International Conference on Multiphase Flow, New Orleans, May 27−June 1,, 2001.
(28) Launder, B. E.; Spalding, D. B. *Lectures in Mathematical Models of Turbulence*. Academic Press: London; New York, 1972.
(29) Yakhot, V.; Orszag, S. A. Renormalization Group Analysis of Turbulence. I. Basic Theory. *J. Sci. Comput.* **1986**, *1* (1), 3–51.
(30) Modeling Turbulence. *Fluent 6.3 - User Guide*.
(31) Paul, E. L.; Atiemo-Obeng, V. A.; Kresta, S. M. *Handbook of Industrial Mixing*; John Wiley and Sons: Hoboken, NJ, 2004.
(32) Rielly, C. D.; Habib, M.; Sherlock, J. P. Flow and Mixing Characteristics of a Retreat Curve Impeller in a Conical-Based Vessel. *Chem. Eng. Res. Des.* **2007**, *85* (7), 953–962.
(33) Davidson, P. A., *Turbulence: An Introduction for Scientists and Engineers*; Oxford University Press: Oxford, 2004.
(34) Pope, S. B., *Turbulent Flows*; Cambridge University Press: Cambridge, 2000.
(35) Saffman, P. G.; Turner, J. S. On the Collision of Drops in Turbulent Clouds. *J. Fluid Mech.* **2956**, No. 1, 16–30.
(36) Abrahamson, J. Collision rates of small particles in a vigorously turbulent fluid. *Chem. Eng. Sci.* **1975**, *30* (11), 1371–1379.
(37) Liew, T. L.; Barrick, J. P.; Hounslow, M. J. A Micro-Mechanical Model for the Rate of Aggregation during Precipitation from Solution. *Chem. Eng. Technol.* **2003**, *26* (3), 282–285.
(38) Modeling discrete phase. *Fluent 6.3 - User Guide*.
(39) Gimbun, J.; Rielly, C. D.; Nagy, Z. K. Modelling of Mass Transfer in Gas−Liquid Stirred Tanks Agitated by Rushton Turbine and CD-6 Impeller: A Scale-Up Study. *Chem. Eng. Res. Des.* **2009**, *87* (4), 437–451.